

Scientific session of the Division of General Physics and Astronomy of the Russian Academy of Sciences (29 January 1997)

A scientific session of the Division of General Physics and Astronomy of the Russian Academy of Sciences (RAS) was held at the P L Kapitza Institute for Physical Problems, RAS on 29 January 1997. Six reports were presented at this session:

(1) **D Bimberg, I P Ipatova, P S Kop'ev, N N Ledentsov, V G Malyshkin, V A Shchukin** (Technische Universität Berlin, Berlin; A F Ioffe Physicotechnical Institute, RAS, St.-Petersburg) “Spontaneous ordering of semiconductor nanostructures”;

(2) **I V Kukushkin** (Institute of Solid State Physics, RAS, Chernogolovka, Moscow region) “Experimental verification of the skyrmion concept”;

(3) **N A Gippius, V D Kulakovskii, S G Tikhodeev** (Institute of General Physics, RAS, Moscow; Institute of Solid State Physics, RAS, Chernogolovka, Moscow region) “Effect of electric field redistribution on the electronic and optical properties of nanostructures”;

(4) **V V Kapaev, Yu V Kopaev, I V Tokatly** (P N Lebedev Physical Institute, RAS, Moscow) “Momentum dependence of electron state dimensionality in heterostructures”;

(5) **V G Lyenko** (Institute of Technology Problems for Microelectronics and Highly Purified Materials, RAS, Chernogolovka, Moscow region) “Bloch oscillations in superlattices”;

(6) **V A Krupenin, S V Lotkhov, Yu A Pashkin, D E Presnov** (M V Lomonosov Moscow State University, Moscow; P N Lebedev Physical Institute, RAS, Moscow) “An experimental study of charge effects in ultrasmall tunnel junctions”.

An abridge version of the five of above reports is given below.

PACS numbers: 68.90.+g, 73.90.+f

Spontaneous ordering of semiconductor nanostructures

D Bimberg, I P Ipatova, P S Kop'ev,
N N Ledentsov, V G Malyshkin, V A Shchukin

1. Introduction

Composition-modulated structures in solid semiconductor solutions along with periodically faceted surfaces, surface structures of plain domains, and ordered arrays of three-dimensional coherently stressed islands are all described

within the unified picture of the equilibrium structures of elastic domains. Although a homogeneous state is unstable for different reasons in different classes of nanostructures, one common factor, the elastic interaction, is responsible for the formation of an ordered structure in the inhomogeneous state.

In this paper we consider spontaneously ordered composition-modulated structures present in epitaxial films of semiconductor solid solutions (Fig. 1a), periodically faceted surfaces (Fig. 1b), periodic structures of plane domains on a surface (Fig. 1c), and ordered arrays of three-dimensional coherently stressed islands in heteroepitaxy systems (Fig. 1d). Since neighbouring domains in all these systems differ in the lattice constants and/or surface structure, domain boundaries act as sources of long-range elastic stress fields. A general approach is proposed, treating all such structures as *equilibrium systems of elastic domains* found at the free-energy minimum. This approach is relevant, for example, to experiments which involve annealing and growth interruption. References to experimental work are given in [1].

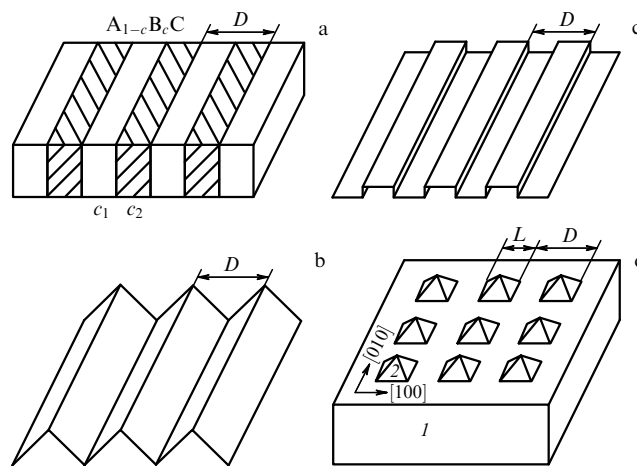


Figure 1. Various classes of spontaneously ordered nanostructures: (a) composition-modulated solid solution structures; (b) periodically faceted surfaces; (c) periodic structures of plane domains; (d) ordered arrays of coherently stressed islands 2 on the substrate 1.

2. Elastic concentration domains in solid semiconductor solutions

The formation of composition-modulated structures in $A_{1-c}B_cC$ solid solutions is due to a homogeneous solid solution being unstable to composition fluctuations $\delta c(\mathbf{r})$. This instability implies that a solid solution with a nonuniform composition profile $c(\mathbf{r}) = \bar{c} + \delta c(\mathbf{r})$ has a lower free energy than its homogeneous counterpart with the composi-

tion $c(\mathbf{r}) = \bar{c}$. The change in the free energy of the system due to composition fluctuations $\delta c(\mathbf{r})$ equals

$$\delta F = \int \left\{ [H(\bar{c} + \delta c(\mathbf{r})) - TS_{\text{mix}}(\bar{c} + \delta c(\mathbf{r}))] - [H(\bar{c}) - TS_{\text{mix}}(\bar{c})] \right\} dV + E_{\text{el}}, \quad (1)$$

where H is the enthalpy, S_{min} is the entropy of mixing, T is the temperature, and E_{el} is the elastic energy. A homogeneous solid solution becomes unstable to composition fluctuations when the enthalpy of the solid solution $A_{1-c}B_cC$ formation from binary components AC and BC is positive: $\Delta H_{\text{form}} \equiv H(A_{1-c}B_cC) - (1-c)H(\text{AC}) - cH(\text{BC}) > 0$. Then for $T = 0$ the two-phase mixture of pure AC and BC has a lower free energy than the homogeneous solid solution $A_{1-c}B_cC$, making this latter unstable. For finite T , the S_{min} contribution to the free energy will aid in mixing the components and stabilizing the homogeneous solid solution.

The elastic energy is due to the equilibrium variation of the lattice constant a of the solid solution with the composition c according to Vegard's rule. Solid-solution regions of various composition show different equilibrium values of lattice constants. Two adjacent regions conjugate via elastic deformation, with which the elastic energy is related. Since $E_{\text{el}} = 0$ in a homogeneous solution and $E_{\text{el}} > 0$ in an inhomogeneous solution, it follows that the elastic energy acts to stabilize the homogeneous solid solution.

The 'soft mode' corresponding to the most unstable composition fluctuations depends on the elastic anisotropy of the crystal and may be viewed as a composition wave with a wave vector parallel to the direction of easiest compression in the crystal [2]. For most cubic materials, these are the [100], [010], and [001]. The final state of a decomposing solid solution is a layered 1D array of elastic concentration domains that alternate along one of the easiest compression directions [3].

The theory of Refs [2, 3] has been extended to epitaxial solid-solution films on the (001) substrate of a cubic crystal matched (with respect to the lattice constant) with a homogeneous solid solution of average composition \bar{c} [4]. It was shown that the 'soft mode' of the composition fluctuations is localized near the free surface $z = 0$ of the film and decays inward exponentially, $\delta c(\mathbf{r}) \propto \exp(-|kz|) \exp(ikx)$, where the wave vector \mathbf{k} is directed along the easiest compression axis [100] (or [010]) in the surface plane. Due to elastic stress relaxation near the free surface, the elastic energy in the 'soft mode' is reduced by a factor of $\simeq 1/3$ from its value in the bulk. The equilibrium composition profile makes

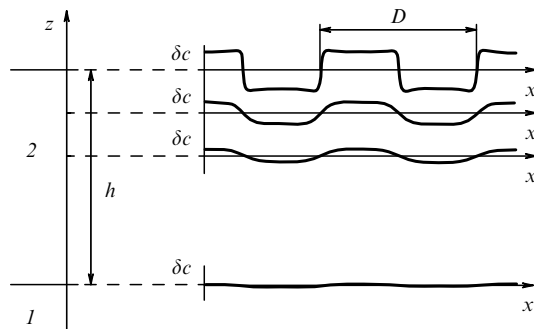


Figure 2. Equilibrium solid-solution composition profile in an epitaxial film 2 on a substrate 1.

a combination of 'soft modes' with different values of \mathbf{k} . The modulation amplitude has a maximum at the free surface of the film and decays inward (Fig. 2), while the composition modulation period D is comparable to the epitaxial film thickness h : $D \simeq h$.

Composition-modulated solid solution structures have been observed in many metal alloys and shown to be equilibrium based on annealing experiments [3]. For semiconductor solid solutions, further experiments are needed to find out whether the observed structures are equilibrium or nonequilibrium by nature.

3. Periodically faceted surfaces

Spontaneously formed periodically faceted surfaces and surface structures of plane domains were treated theoretically by Andreev [6] and Marchenko [5, 7]. As we rely heavily on their theory in our analysis of arrays of three-dimensional stressed islands, a brief outline is appropriate here.

The spontaneous faceting of crystal plane surfaces is due to the orientation dependence of the surface free energy. If the specific surface energy of the plane surface is large, then it transforms spontaneously to the 'hill-and-valley' structure (Fig. 1b), which lowers the total free energy of the surface even though its area increases.

Since the surface tension tensor τ_{ij} is different for neighbouring faces, a jump in its value occurs at the edges between faces. It is this jump of τ_{ij} tensor which gives rise to elastic strain fields.

For a periodically faceted surface of period D , the total free energy per unit area of the originally plane surface equals [5]

$$F = F_{\text{surf}} + E_{\text{edges}} + \Delta E_{\text{el}}, \quad (2)$$

where $F_{\text{surf}} = \text{const}(D)$ is the surface free energy of the tilted faces, $E_{\text{edges}} = C_1 D^{-1}$ is the short-range component of the edge energy, and $\Delta E_{\text{el}} = -C_2 D^{-1} \ln(D/a)$ is the elastic relaxation energy. Because the strains are exerted by linear sources (edges), ΔE_{el} varies logarithmically with D . Therefore, free energy (2) always has a minimum at a certain optimal period $D_{\text{opt}} = a \exp[C_1/C_2 + 1]$.

4. Surface structures of plane domains

Plane domain structures are generated on a surface on which different phases, such as reconstruction phases (2×1) and (1×2) on Si(001), monolayer islands in heterophase systems, etc., may coexist [6]. Adjacent domains then have different values of the surface tension tensor τ_{ij} , thus leading to elastic relaxation. The total energy of a system of plane domains equals [7]

$$E = E_{\text{surf}} + E_{\text{bound}} + \Delta E_{\text{el}}. \quad (3)$$

The surface energy E_{surf} is independent of the structure period D , the domain boundary energy is $E_{\text{bound}} = C_1 D^{-1}$, the elastic relaxation energy is $\Delta E_{\text{el}} = -C_2 D^{-1} \ln(D/a)$, and the total energy (3) always has a minimum at a certain optimal period D_{opt} . Thus, it is the elastic relaxation due to the jump in τ_{ij} at domain boundaries which causes the generation of surface structures based on plane domains.

5. Ordered arrays of three-dimensional coherently stressed islands

The formation of 3D coherently stressed islands in mismatched heteroepitaxy systems is due to the bulk elastic relaxation, i.e. to the fact that island formation reduces the

elastic energy compared to that of a uniformly stressed epitaxial film [8]. In a 3D array of islands there appear two sources of elastic deformations: first, the lattice constant mismatch between the island and substrate materials, and, second, the jumps in the surface tension tensor at the island edges. Thus, the change in the total energy of the system due to the formation of a single coherently stressed island of linear dimension L equals

$$\tilde{E}_{\text{isl}} = \Delta\tilde{E}_{\text{el}}^{\text{V}} + \Delta\tilde{E}_{\text{surf}} + \tilde{E}_{\text{edges}} + \Delta\tilde{E}_{\text{el}}^{\text{edges}}. \quad (4)$$

Here $\Delta\tilde{E}_{\text{el}}^{\text{V}} \propto -L^3$ is the bulk elastic relaxation energy; $\Delta\tilde{E}_{\text{surf}} \propto \pm L^2$ is the change in the surface free energy due to the formation of tilted island faces, the disappearance of the plane surface, and the development of an interface between the 3D island and the substrate; the latter quantity may have either sign; $\tilde{E}_{\text{edges}} \propto L$ is the short-range energy contribution from the edges, and $\Delta\tilde{E}_{\text{el}}^{\text{edges}} \propto -L \ln L$ is the contribution from the island edges to the elastic relaxation energy.

For a rarefied island array, the energy per unit area comprises $E = N\tilde{E}_{\text{isl}}$, where N is the island concentration. Equilibrium conditions imply that islands can exchange atoms by means of surface migration, the total amount of material in all the islands being fixed, $NL^3 = \text{const}$. Then the energy of the island array per unit area is $E \sim \tilde{E}_{\text{isl}}L^{-3}$ and its dependence on the island size L follows from (4) as

$$E = -\text{const} + \frac{C_0}{L} + \frac{C_1}{L^2} - \frac{C_2}{L^2} \ln\left(\frac{L}{a}\right). \quad (5)$$

The relation between E_{edges} and $\Delta E_{\text{el}}^{\text{edges}}$ [the third and fourth terms in (5)] sets the characteristic length scale of the problem, $L_0 = a \exp(C_1/C_2 + 1/2)$. The dependence of E on L in (5) differs considerably from the faceted case because the surface energy ΔE_{surf} depends on the island size L . The function $E(L)$ shown in Fig. 3 behaves differently depending on the parameter $\alpha = \exp(1/2)C_0L_0/C_2$. For $\alpha > 1$, the absolute minimum of energy is approached asymptotically as $L \rightarrow \infty$. This means that the system tends to decrease its total surface area, and the whole of the deposited material

gathers into a macroscopic cluster, i.e. a coalescence occurs. For $\alpha \leq 1$, the absolute minimum of energy E is achieved at a finite island size L_{opt} , implying the formation of single-sized islands and no coalescence [9, 10]. Of particular interest is the case of $\alpha < 0$, in which island formation is followed by a decrease not only in the elastic energy but also in the *surface energy of the system*. Notice that the minimum in the energy $E(L)$ obtained for the rarefied island array is also conserved for a dense array, with the elastic interaction between the islands taken into account [10].

The ordering of islands in a plane is due to the elastic island-island interaction. It has been shown [10] that, of various possible arrays on the (001) surface of elastically anisotropic cubic crystal, one minimizing the elastic energy is the *periodic square lattice* with unit cell vectors lying along the easiest compression directions [100] and [010] (Fig. 1d).

The theory agrees well with the experimental data [11] on the spontaneous formation of an InAs island array on the GaAs(001) surface, where the islands have the same (pyramidal) shape and a narrow size distribution, and each of them has four nearest neighbours as is typical for a square lattice, thus indicating the presence of a short-range order in the system.

The distinguishing feature of 3D arrays of coherently stressed islands as compared to other nanostructure classes is that for island arrays both the island-ordering and coalescence regimes are possible. Accordingly, a crossover from the former to the latter may be realized — for example, by varying the pressure in As and thereby all the surface energies in the system. Such a phase transition from the ordering regime to the coalescence regime has been identified experimentally [12].

6. Conclusion

Theoretical approaches to the spontaneous formation of periodic nanostructures have been reviewed within a unified framework in which a number of nanostructure classes are considered as equilibrium structures of elastic domains. For all of them the ordering mechanism is due to long-range elastic forces, with elastic anisotropy often determining the way the domain array is spatially oriented relative to the crystal axes. The phenomena of spontaneous ordering of nanostructures find wide application in the technology of quantum wire and quantum dot superlattices.

The support of the RFBR through Grant No 96-02-17943a, State Program ‘Solid State Nanostructures Physics’ (Grant No 2-001), and Deutsche Forschungsgemeinschaft (Sfb 296) is gratefully acknowledged.

References

1. Shchukin V A, in *Proc. 23rd Int. Conf. Phys. Semicond., July 22–26 1996, Berlin, Germany* Vol. 2 (Eds M Scheffler, R Zimmermann) (Singapore: World Scientific, 1996) p. 1261
2. Cahn J W *Trans. Metall. Soc.* **242** 166 (1968)
3. Khachaturyan A G *Theory of Phase Transformations in Solids* (New York: John Wiley and Sons, 1983)
4. Ipatova I P, Malyskin V G, Shchukin V A *J. Appl. Phys.* **74** 7198 (1993), *Phil. Mag. B* **70** 557 (1994)
5. Marchenko V I *Zh. Eksp. Teor. Fiz.* **81** 1141 (1981) [*Sov. Phys. JETP* **54** 605 (1981)]
6. Andreev A F *Pis'ma Zh. Eksp. Teor. Fiz.* **32** 654 (1980) [*JETP Lett.* **32** 640 (1980)]
7. Marchenko V I *Pis'ma Zh. Eksp. Teor. Fiz.* **33** 397 (1981) [*JETP Lett.* **33** 381 (1981)]

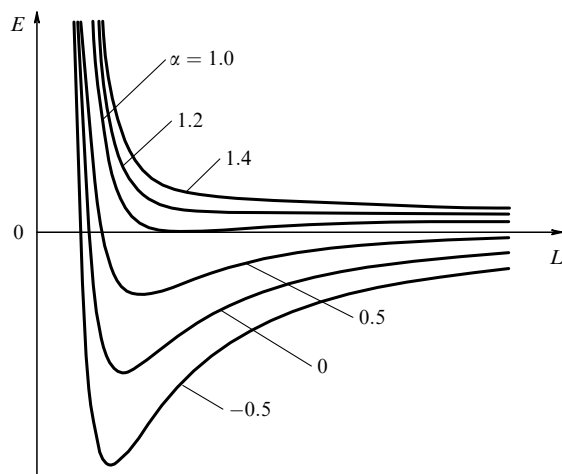


Figure 3. Energy per unit surface area vs. island size for a rarefied array of three-dimensional coherently stressed islands. Parameter α is the ratio of the island-formation surface energy change to the island edge contribution to the elastic relaxation energy. If $\alpha > 1$, the islands coalesce. For $\alpha \leq 1$, the island size has an optimum and no coalescence occurs.

8. Vanderbilt D, Wickham L K *MRS Proc.* **202** 555 (1991)
9. Shchukin V A et al. *Surf. Sci.* **352–354** 117 (1996)
10. Shchukin V A et al. *Phys. Rev. Lett.* **75** 2968 (1995)
11. Grundmann M et al. *Phys. Rev. Lett.* **74** 4043 (1995)
12. Ledentsov N N et al. *Solid State Electron.* **40** 785 (1996)

PACS numbers: 12.39.Dc, 73.40.Hm

Experimental verification of the skyrmion concept

I V Kukushkin

In Laughlin's theory [1] of the fractional quantum Hall effect (FQHE) for the filling factor $\nu = 1/m$ (with m being an odd integer), electron states are deemed to be fully spin polarized. However, as was first noted in [2], in a weak magnetic field it may happen that in some FQHE states, because of the small electron g -factor, an energy minimum will correspond to an electron system without spin polarization. This has been verified by numerical calculations [3, 4] which show that in the zero-Zeeman-energy limit the ground state of an electron system may correspond to both a complete, and partial or zero spin polarization at various fractional values of the filling factor. The exchange-correlation energy competition was indicated as the reason why ground states may have different spin polarizations in various FQHE states [5]. Although this theoretical discordance has been indirectly confirmed by transport-related activation gap measurements in a canted magnetic field [6, 7], thus far no direct experimental method has been available to measure the spin polarization coefficient of an electron system in various FQHE states.

The appearance [8, 9] and experimental confirmation [10] of the skyrmion theory have recently given an impetus to studies on the spin polarization of two-dimensional electron systems in a perpendicular magnetic field. In this theory, although the ground state at $\nu = 1$ and low g -factor is fully spin-polarized, even a slight deviation from the full filling causes a strong depolarization. The ground state of the electron system with ν close to 1 and an extra electron with reversed spin does not imply a single reversed spin but rather corresponds to a macroscopically large spin defect which secures a smooth rotation of the spin field from the antiparallel to the parallel spin. Such a defect is referred to as the 'skyrmion' [8]. The size of the skyrmion depends on the competition between the Coulomb interaction energy and the Zeeman energy and increases logarithmically as the electron g -factor tends to zero [8]. Due to a small value of the electron g -factor in GaAs ($g = -0.44$), two-dimensional systems appear to be good candidates for skyrmion excitations, especially in weak-magnetic-field experiments, when the Zeeman energy is small compared to the Coulomb energy.

The method we employ here involves an analysis of the circular polarization for the radiative recombination of two-dimensional electrons with photoexcited holes bonded to acceptors. This approach allows a direct measurement of the spin polarization coefficient of the electron system in various FQHE states and near $\nu = 1$. It is found that in weak magnetic fields some fractional states possess no spin polarization and it is also shown that with increasing magnetic field the electron spin polarization in these states grows from zero to unity. Although there is no evidence for the existence of skyrmion excitations in a strong magnetic

field limit ($B > 4$ T), the spin depolarization of the electron system observed in small magnetic fields ($B < 2$ T) near $\nu = 1$ indicates that skyrmions require the suppression of the Zeeman energy for their existence.

The present study was made on a group of high-quality single GaAs/AlGaAs heterojunctions [mobility of two-dimensional electrons ranged $(0.5-2) \times 10^6$ cm² (V s)⁻¹ at densities of $(0.28-2.4) \times 10^{11}$ cm⁻²] with a Be-acceptor monolayer placed distance 300 Å from the interface [11]. We used titanium-sapphire laser pulses of wavelength of about 800 nm, duration 20 ns, and peak power of 0.1 mW cm⁻² to create photoexcitation and a photon counting system to detect time-resolved luminescence spectra. For a spectral apparatus we employed the double monochromator Ramanor U-1000 with a resolving power of 0.03 meV. The circular luminescence polarization at low temperatures (up to 30 mK) was analyzed using a light guide optical system with a linear polarizer and a $\lambda/4$ plate located in the solution cryostat between the sample and the light guide. With this system, σ^+ - to σ^- -polarization signal ratios of up to 100 (corresponding to the depolarization coefficient of 0.02) could be measured.

Figure 1 shows the luminescence spectra for σ^+ - and σ^- -polarizations measured for $\nu = 5$ ($B = 1.95$ T) and two different temperatures (0.6 and 1.0 K). It is seen that the degree of the circular luminescence polarization is determined by the temperature and is markedly varied for fully occupied (two low-energy lines) and spin-polarized (the high-energy line) levels. The important point to note is that the temperature determining the degree of the circular luminescence polarization corresponds to the effective temperature of hole photoexcitation and it was therefore crucial for us that the hole system be in thermal balance with the helium thermostat. This was achieved via the time resolution technique by examining the luminescence spectra measured with a long time delay para to the photoexcitation pulse. That the time delay was taken to be much longer than the energy relaxation time for the photoexcited holes ensured that the holes cooled down to the bath temperature. Notice that this relaxation time, relatively short at high temperatures (1 to 3 ns at 4 K [12]), grows significantly with cooling and is close to 100 ns at 0.5 K — the reason why the time delay was typically in the range 300 to 600 ns in our measurements.

There are two independent factors determining the degree of circular polarization of the radiative recombination of two-

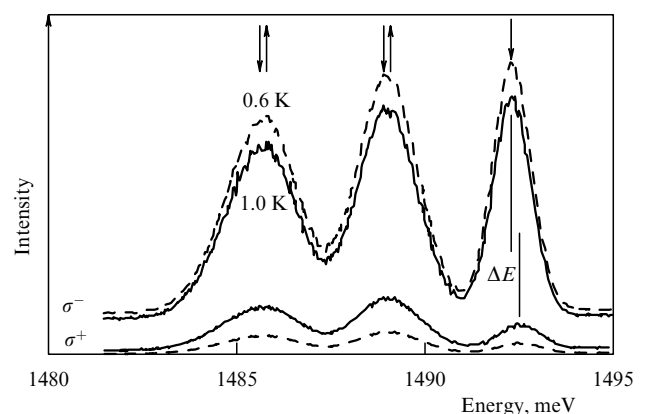


Figure 1. Luminescence spectra at $B = 1.95$ T ($\nu = 5$) for σ^+ - and σ^- -polarisations at $T = 1.0$ K and 0.6 K measured with a 300-ns delay after the photoexcitation pulse.

dimensional electrons with acceptor-bonded photoexcited holes. First, these holes become spin-polarized due to the Zeeman effect, the degree of polarization being determined by the magnetic field and the hole temperature (i.e. by the population of the Zeeman hole sublevels). The second factor is the spin polarization of the two-dimensional electrons, dependent primarily on the filling factor and the temperature. Since these two factors are experimentally separable and can be examined independently [13], the contribution from the spin polarization of the electron system can be decoupled through the analysis of the circular luminescence polarization.

Using this method, the degree of circular luminescence polarization and the degree of spin polarization of two-dimensional electrons were obtained as functions of the magnetic field for three samples with a low density of two-dimensional electrons (see Fig. 2). For one of the samples, a comparison between the magneto-optical and transport data was carried out which indicated that the $5/3$, $4/3$, $2/3$, $3/5$, and $2/5$ FQHE states show up in both the magnetoresistance and the electron spin polarization, virtually all of these states (except for $5/3$ [13]) being not fully polarized for spin. On the contrary, the electron spin polarization at $\nu = 2/3$ and

$B = 1.8$ T, for example, is only 0.1, while for FQHE states at $\nu = 3/5$ and $\nu = 2/5$ it is close to 0.3 (in 2 T and 3 T fields, respectively).

As seen in Fig. 2, increasing the magnetic field to 3–4 T markedly adds to the electron spin polarization in all of the FQHE states studied. For $B > 3$ T, the $\nu = 3/5$ and $\nu = 2/5$ states become completely spin polarized, and the degree of spin polarization at $\nu = 2/3$ grows with the magnetic field, reaching 0.5 at $B = 2.7$ T and 0.9 at 3.4 T. Although the observed behaviour of the spin polarization of two-dimensional electrons in various FQHE states is qualitatively consistent with theory, experimentally the transformation of the spin polarization of fractional states occurs at magnetic fields much weaker than predicted by the theory [4]. This discrepancy is most likely due to the neglect of theoretical corrections for the finite width of the two-dimensional channel.

Measuring the spin polarization of a two-dimensional electron system as a function of the filling factor near $\nu = 1$ may serve as a direct experimental test for the skyrmion theory. That the electron spin polarization for $B > 3$ T and $\nu < 1$ is close to 1 (see Fig. 2) is clearly inconsistent with the skyrmion model in which the skyrmion has a noticeable size of about three magnetic lengths (total spin of about 3) for $g = -0.44$ and $B = 7$ T [8] thus suggesting a marked spin depolarization at $\nu < 1$. Under certain experimental conditions, however, an effective spin depolarization of the electron system close to both the theoretical predictions and the measured data of Ref. [10] was obtained at about $\nu = 1$. Figure 3a shows the magnetic-field dependence of the spin polarization of the two-dimensional electrons as measured near $\nu = 1$ under normal conditions (open circles) and for a heating electric current ($j = 30 \mu\text{A}$) passed through the system of two-dimensional electrons (closed circles). It is seen that under normal conditions the system is completely spin polarized at $\nu < 1$ and that heating by a 30- μA current, while leading to an effective spin depolarization at both $\nu < 1$ and $\nu > 1$, practically does not affect the electron polarization at $\nu = 1$. The explanation is that the Ohmic heating of electrons in the electric field is proportional to the diagonal resistivity ρ_{xx} (the Joule power $W = j^2 \rho_{xx}$), and since ρ_{xx} reaches a minimum at $\nu = 1$, so does the effective heating of two-dimensional electrons. A similar effect observed in transport measurements for both even and odd integer filling factors is called the QHE breakdown [14] and is one-particle in nature. Although the electric-current-induced spin depolarization observed near $\nu = 1$ is most unlikely connected with skyrmion excitations (which are due to the Coulomb interaction), effects like these still have to be considered in interpreting the experimental data.

In weak magnetic fields ($B < 2$ T), the electron system was observed to be spin-depolarized near $\nu = 1$, but this may be due in part to the presence of $2/3$ and $3/4$ states which, as discussed above, possess a nonpolarized ground state in weak fields. The dependence of the electron spin polarization on the filling factor is shown in Fig. 3b for three different samples of very low electron density, in which the $\nu = 1$ filling was achieved at $B = 2.3$, 1.15, and 0.8 T, respectively. Weak field measurements are particularly interesting in that in this case a reduced Zeeman (E_Z) to Coulomb (E_C) energy ratio — and hence stronger skyrmion effects — are expected. As it can be seen from Fig. 3b, decreasing the field from 2.3 T to 1.15 T (at $\nu = 1$) leads to virtually complete spin depolarization in the $2/3$ and $4/3$ states. In a weaker field ($B = 0.8$ T,

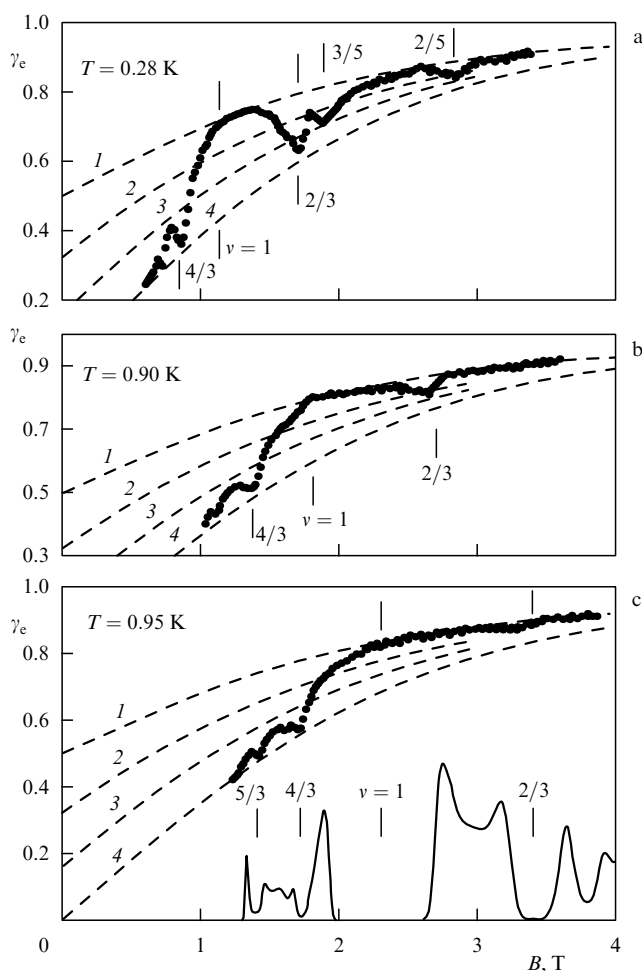


Figure 2. Variation of the degree of circular luminescence polarization for three samples with low density of two-dimensional electrons: $2.8 \times 10^{10} \text{ cm}^{-2}$ (a); $4.4 \times 10^{10} \text{ cm}^{-2}$ (b); $5.5 \times 10^{10} \text{ cm}^{-2}$ (c). For comparison, magnetotransport oscillations measured in one of the samples at $T = 70$ mK are also shown. Dashed curves represent calculations for the various values of electron spin polarization: 1 — 100%, 2 — 67%, 3 — 33%, 4 — 0%.

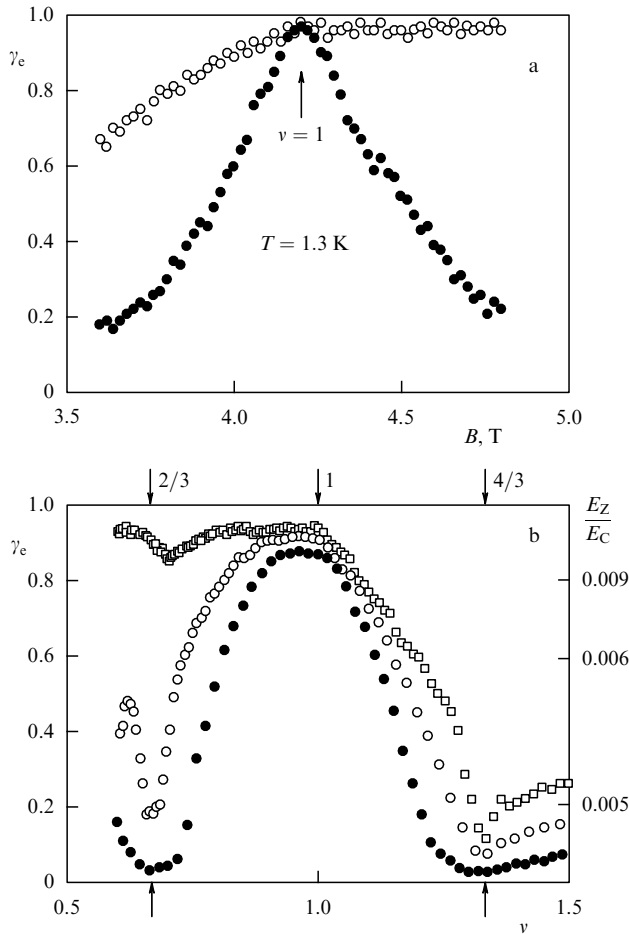


Figure 3. (a) Spin polarization of two-dimensional electrons as a function of the magnetic field induction, measured near $\nu = 1$ in the presence ($j = 30 \mu\text{A}$, closed circles) and in the absence ($j = 0$, open circles) of a heating electric current. (b) The degree of electron spin polarization as a function of the filling factor for three samples at $\nu = 1$ (figure shows the Zeeman to Coulomb energy ratio realized in these samples at $\nu = 1$). Dashed line represents the behaviour expected from the one-particle theory.

$\nu = 1$) these spin polarization minima are broadened at $\nu = 4/3$ and $\nu = 2/3$ such that a significant spin polarization only survives for filling factors in a narrow region near $\nu = 1$. This weak-field behaviour of the spin polarization may be interpreted as being due to skyrmion excitations and is indicative of the fact that the skyrmion model describes the ground state of an electron system adequately only when the Zeeman energy is strongly reduced. Since, as is well known, the g -factor of electrons in GaAs can be reduced to zero by applying the hydrostatic pressure, further work on skyrmion effects requires magneto-optical measurements to be made under pressure in which, by smoothly varying the electron g -factor, an unbounded increase in both the size and the effective spin of skyrmions could be obtained.

This work was supported by the ‘Solid-State Nanostructure Physics’ Program through Grant No 1-062/3 and by INTAS through Grant No 95-IN/RU-675.

References

1. Laughlin R B *Phys. Rev. Lett.* **50** 1395 (1983)
2. Halperin B I *Helv. Phys. Acta* **56** 75 (1983)

3. Chakraborty T, Zhang F C *Phys. Rev. B* **29** 7032 (1984)
4. Zhang F C, Chakraborty T *Phys. Rev. B* **30** 7320 (1984)
5. Maksym P A *J. Phys.: Condens. Matter* **1** 6299 (1989)
6. Eisenstein J P et al. *Phys. Rev. Lett.* **62** 1540 (1989)
7. Clark R G et al. *Phys. Rev. Lett.* **62** 1536 (1989)
8. Sondhi S L et al. *Phys. Rev. B* **47** 16419 (1993)
9. Fertig H A et al. *Phys. Rev. B* **50** 11018 (1994)
10. Barrett S E, Pfeiffer L N, Tycko R *Phys. Rev. Lett.* **74** 5112 (1995)
11. Kukushkin I V et al. *Phys. Rev. B* **40** 7788 (1989)
12. Filin A I et al. *Pis'ma Zh. Eksp. Teor. Fiz.* **56** 160 (1992) [*JETP Lett.* **56** 156 (1992)]
13. Kukushkin I V, Klitzing K, Eberl K *Phys. Rev. B* (in press)
14. Ebert G et al. *J. Phys. C* **16** 5441 (1983)

PACS numbers: 73.90.+f, 78.66.-w

Effect of electric field redistribution on the electronic and optical properties of nanostructures

N A Gippius, V D Kulakovskii, S G Tikhodeev

1. Introduction

The behaviour of superlattice and quantum-well semiconductor nanostructures on the base of GaAs/AlGaAs and InGaAs/GaAs heterojunctions depends heavily on the spatial localization of electrons and holes [1]. The dielectric constant difference is too small to produce any significant effects (except for the distributed Bragg mirrors and micro-resonators on their base [2]). However, nanostructures exist whose permittivity variations rather strongly affect the electronic and optical properties of the material. These are, first and foremost, superlattices and quantum wells with strongly different layer permittivities (such as InGaN/GaN [3] and GaAs/ZnSe [4] structures) and semiconductor/insulator (e.g., semiconductor/oxide [5]) structures. Some of the important realizations of such nanostructures are semiconductor nanocrystals [6] or quantum filaments [7] in a dielectric matrix, and also porous silicon [8]. For subsurface quantum wells [9] and for open quantum filaments and quantum dots fabricated from such wells by nanolithography [10–12], the small value of the permittivity of vacuum as compared to the semiconductor permittivity is a crucial factor. In all such structures the difference in permittivities of neighbouring nanostructure regions results in a redistribution of the electric component of the local electromagnetic field (for example, an emitted or absorbed wave, the electron-hole binding field with creation of exciton, etc.). It is the purpose of this work to analyze (a) the light polarization properties for absorption, emission, and scattering by anisotropic structures like open semiconductor quantum filaments or nonspherical nanocrystals in a dielectric matrix, (b) the image-charge-interaction-related exciton enhancement, and (c) the effect of permittivity nonlocality on the polariton modes.

As a consequence of the standard boundary conditions for the normal and tangential electric field components

$$\varepsilon_1 E_{1n} = \varepsilon_2 E_{2n}, \quad E_{1t} = E_{2t}, \quad (1)$$

the electromagnetic field present in the nanostructure undergoes a redistribution if $E_n \neq 0$. The necessity of including the nonlocal response and a complex geometry of the nanostructure dramatically complicates the theoretical analysis of

the problem. In some cases however, where, say, the nanostructure dimensions are much less than the wavelength of light, or in the exciton problem (in which low-frequency and small-wave-vector response is important), the quasi-electrostatic approach is adequate enough to rely upon.

2. Absorption, photoluminescence, and Raman scattering polarization in quantum filaments

The strong linear polarization of photoluminescence from quantum filaments bordering vacuum was first discovered in Ref. [13]. Attempts to explain the effect by the anisotropy of the dipole matrix element have proved a failure [14]: for realistic filament sizes, the calculated degree of linear polarization did not exceed 5–10%, to be compared with experimental values of up to 60–70% [15]. At the same time, for perpendicular light polarization (the electric wave component is normal to the filament axis) and also in the presence of a difference between the filament and the host material permittivities, the electric field will clearly be nonuniform, specifically weakening within the filament where transitions of interest, involving the absorption, emission, or scattering of light, take place. As a result, in the transition region the local effective electric field of the wave depends on its orientation relative to the filament, and the absorption, emission, and scattering of light occur with different probabilities for polarizations along and perpendicular to the filament [16]. The well-familiar dependence of the molecular spontaneous radiation probability on the permittivity of ambient particles [17] is in fact of the same nature (see also [18] and references therein).

If the filament has a transverse dimension which is small compared with the wavelength of light, the electric field distribution in it can be found by solving the electrostatic Poisson equation $\nabla^2 \mathbf{E} = 0$ with the boundary conditions (1). For parallel polarization, clearly no field redistribution occurs. The distribution in the perpendicular case is illustrated in Fig. 1 for two quantum filaments of rectangular cross section and different height-to-width ratios h/w . Neglecting for the sake of simplicity the dipole moment anisotropy (which will not introduce an error as large as 5% in the case of filaments around the InGaAs quantum wells [14]), the linear absorption (emission) polarization coefficient

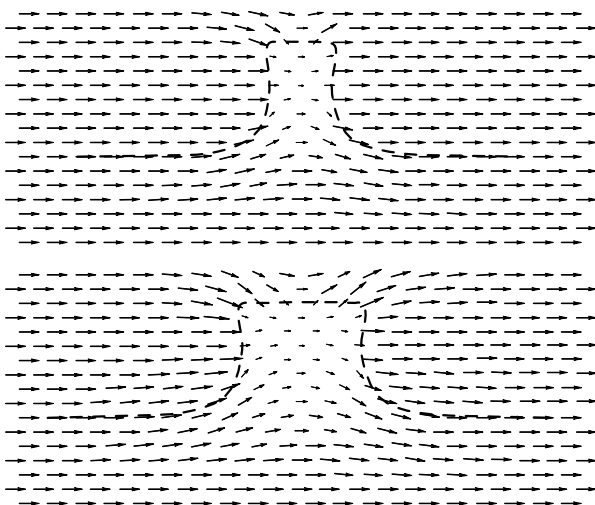


Figure 1. Spatial distribution of the electric field in an open quantum filament (after [19]).

in the dipole approximation is defined as

$$\sigma \simeq \frac{\langle E_{\parallel} \rangle^2 - \langle E_{\perp} \rangle^2}{\langle E_{\parallel} \rangle^2 + \langle E_{\perp} \rangle^2}, \quad (2)$$

where E is the correspondingly-polarized local field strength averaged over the wave functions of the filament-confined electrons and holes. From (2) and the electric field distribution in the filament (Fig. 1) it is evident that the degree of polarization increases with h/w and depends on the position of the localization region within the filament. Theoretical evaluations for open InGaAs/GaAs and InGaAs/InP filaments using formula (2) are in excellent agreement with the experimental data [19] on the linear exciton-photoluminescence polarization (see Fig. 2, where structure cross sections are also shown schematically).

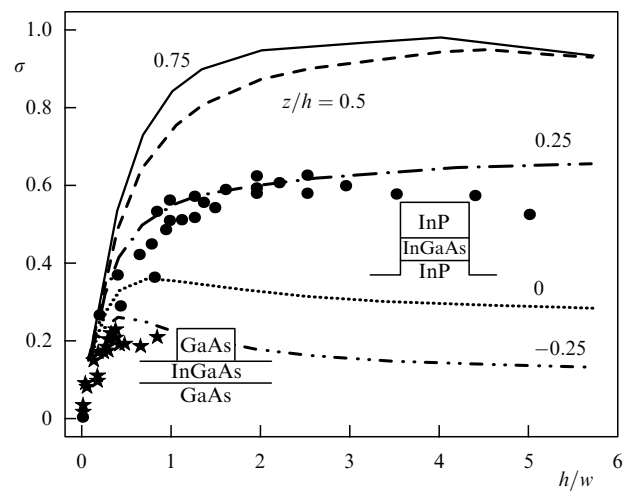


Figure 2. The degree of linear polarization of photoluminescence from open quantum filaments as a function of the height-to-width ratio for various positions z of the carrier localization region: theory and experiment (after [19]). Structure sections are shown schematically next to the corresponding data points.

Turning now to the Raman scattering of light in a filament, this process involves two photons, and in the dipole approximation we have instead of (2) the relationship [20]

$$\sigma_{\text{Raman}} \simeq \frac{\langle E_{\parallel} \rangle^4 - \langle E_{\perp} \rangle^4}{\langle E_{\parallel} \rangle^4 + \langle E_{\perp} \rangle^4}. \quad (3)$$

Thus Raman scattering should be even more polarization dependent, which agrees well with the measurements of Ref. [20] (see Fig. 3) on the same structures. A strong linear photoluminescence polarization of a presumably similar nature was also seen in open CdTe/ZnTe filaments [11]. It is to be emphasized that this effect has nothing to do with the diffraction grating effect [21] and occurs for isolated filaments as well as for their random arrays provided the filament separation is much greater than w, h .

Notice also that these polarization effects are not of course limited to quantum filaments but may also be observed in any set of anisotropic semiconductor nanostructures found in a dielectric matrix. Thus, this effect accounts for the strong photoluminescence polarization properties of porous silicon [22] if one assumes this material to be an ensemble of nonspherical nanocrystallites embedded in a

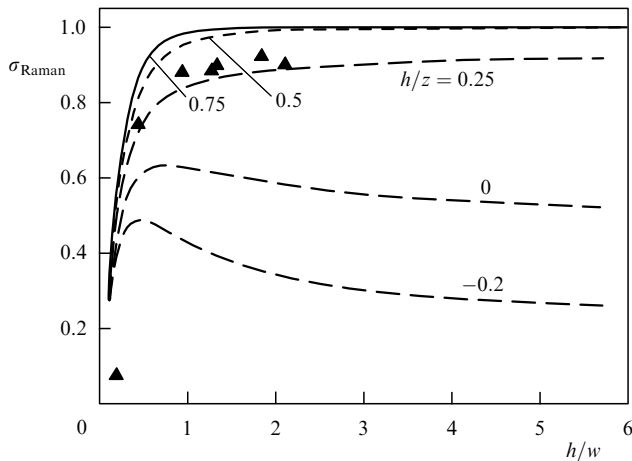


Figure 3. The behaviour of the degree of linear polarization of Raman scattering from open quantum filaments: theory and experiment (after [20]).

dielectric matrix [23, 24]. In particular, the experimental angular behaviour of the intensity of polarized photoluminescence has been shown [24] to depend on exactly how the shapes and orientations of nanocrystallites are distributed over a porous silicon sample. By comparison with experiment, the nanocrystallite distribution function was partially reconstructed.

Polarization effects of the type discussed enable relatively simple nondestructive measurements of the geometrical parameters of open nanostructures to be made — not always an easy task, especially if the region of spatial localization of the electronic transition is to be determined.

3. Dielectric enhancement of excitons

The binding energy of excitons in semiconducting films and semiconductor/insulator quantum wells greatly exceeds that of three-dimensional excitons in corresponding bulk semiconductors. In such systems, in addition to dimensional quantization which renders the exciton quasi-two-dimensional (thus increasing the binding energy by at most† 4 times [1]), a crucial role in determining the electron-hole interaction is also played by the image potentials that result from the large permittivity difference between the semiconductor and the insulator (or vacuum in the case of semiconducting films). Image potentials cause a marked increase in the electron-hole attraction, and as a consequence, produce stronger excitons (the so-called dielectric confinement or dielectric enhancement of excitons) [26–28].

In a semiconductor quantum filament (or dot) embedded in a dielectric, an electron and a hole find themselves even more strongly bound because their dielectric surrounding is larger compared to the planar well case. The exciton enhancement effect has been treated in detail theoretically for a variety of structure types (see, e.g., [29–38] and the review [38]). Although the change in the binding energy has been observed in thin semiconductor (CdTe) films on the dielectric substrate [39], its detailed study was significantly hindered by the complexity of the absorption spectra observed.

† Since the Coulomb binding energy is infinite in the one-dimensional case [25], quasi-one-dimensional spatial localization may be stronger.

Later, more detailed studies on self-organizing lead-iodide-based semiconductor/insulator superlattices were carried out [40–43]. These intercalation structures, in which variously shaped semiconducting lead-iodide layers are surrounded by various organic (dielectric) compounds, represent an extremely diverse family of structures like superlattices based on dielectric-matrix-embedded quantum wells, filaments, and dots [44]. With increasing spatial localization the exciton binding energy in these structures grows from about 45 meV in a pure semiconductor to 300 meV in quantum wells, 700 meV in quantum filaments, and upwards of 1 eV in quantum dots [44], primarily due to the effect of the dielectric surrounding [37, 45]. However, because of the small size of the exciton (of the order of 3 interatomic distances), the Wannier–Mott approximation in such structures is at the applicability boundary, and predictions of the dielectric model are in fact no more than qualitative in nature. Recently, many growth techniques have been proposed for high-quality semiconducting quantum filaments in pores in dielectric materials — for example, GaAs filaments in asbestos nanotubes [7] (for theoretical estimations of exciton parameters in such filaments, see [45]).

Recently it has been found [46, 47] that InGaAs/GaAs quantum wells near the vacuum interface hold considerable promise for the study of the dielectric enhancement of excitons. This structure is the simplest realization of a system in which dielectric permittivity varies very strongly — indeed by more than an order of magnitude — in the immediate vicinity of an exciton. In Ref. [46], the diamagnetic coefficient of the 1s-level and the frequencies of the 1s- and 2s-exciton transitions were measured as functions of the thickness of the well-vacuum barrier layer using photoluminescence and photoexcitation spectra. And it was found that the exciton strengthens significantly as the barrier thickness is decreased, which is in good quantitative agreement with calculations taking account of the interaction of carriers with their images. In Ref. [47], the behaviour of excitons in a subsurface well in a perpendicular magnetic field $B < 14$ T was studied both experimentally and theoretically. The magnetic field enables the exciton state size to be controlled and thus the effect of dielectric enhancement of the exciton to be quantitatively examined.

A system involving a quantum well near the surface has proved to be a very convenient model with which to vividly demonstrate the effects leading to exciton enhancement and on which to rely in carrying out detailed experimental studies of these effects. The dielectric enhancement of the exciton binding energy may be interpreted as being due to an additional attraction that arises between the electron and the hole image and between the hole and the electron image. (Recall that if a charge e finds itself in a medium with permittivity ε near a plane interface with a medium possessing the refraction index ε_1 , then the charge of the image equals

$$e' = \frac{\varepsilon - \varepsilon_1}{\varepsilon + \varepsilon_1} e, \quad (4)$$

i.e. its sign is the same as that of the charge, provided $\varepsilon > \varepsilon_1$). In terms of the position of exciton lines in the absorption spectrum, it would seem that increasing a binding energy will shift them towards the red (i.e. to lower exciton transition energies). In actual fact, however, exciton lines must always shift towards the violet! The reason is that apart from the attraction between the electron and the hole image (and vice

versa), the electron and the hole are also repelled by their own images (the so-called self-action effect [31]), and because a charge is always closer to its own image than to that of any other charge, the net effect is that the repulsion dominates over the attraction.

Changes in the one-particle potential profiles of a subsurface quantum well have been obtained by allowing for the self-action forces and are shown schematically in Fig. 4. Figure 5a for a subsurface InGaAs/GaAs quantum well illustrates the theoretical prediction of how the transition energy between unbound electrons and holes (the upper two curves) and the energy of 1s-exciton transition behave as the thickness of the barrier layer between the quantum well and vacuum decreases (dashed curves have been calculated by neglecting the image charge effect). It is seen that the violet shift of the energy of transition between free carriers is dominated by the self-action. For the exciton transition, the violet shift is primarily due to tunnelling (i.e. to the wave function localization by the high vacuum-produced potential barrier). The electrostatic interaction is virtually suppressed because of the electrical neutrality of the exciton (the only remaining force is the weak dipole repulsion from the interface with the vacuum). It is clearly impossible to identify the exciton enhancement effect experimentally from the 1s-transition shift (see experimental points in Fig. 5a) and one should therefore measure the binding energies of exciton states in a direct way. Experimentally, however, the splitting between the 1s- and 2s-lines is easier to measure (because the exciton ionization energy is hard to identify in practice). As shown in Fig. 5b, this splitting increases as the barrier layer thickness decreases — primarily due to the dielectric enhance-

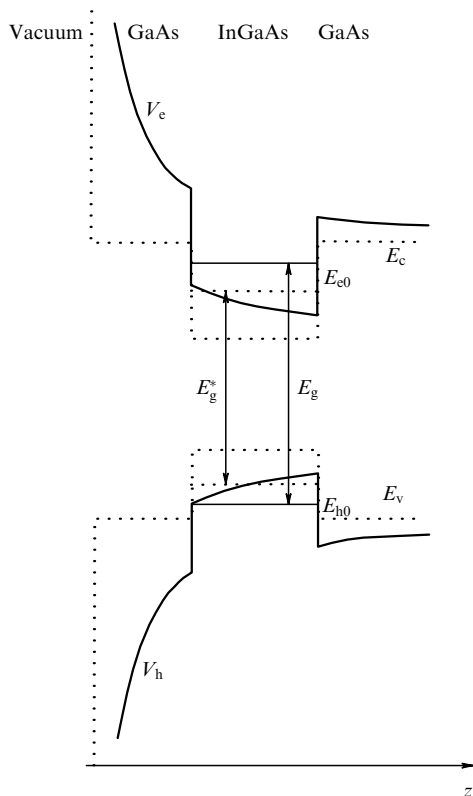


Figure 4. Changes in localizing potentials and one-particle level positions in a subsurface quantum well with (solid lines) and without (dotted lines) allowance made for self-action (after [46]).

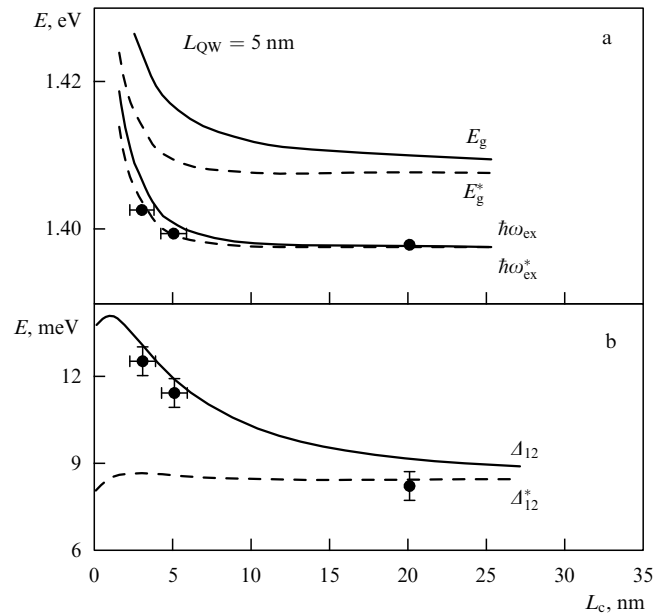


Figure 5. (a) Positions of the band bottom energy $E_g(E_g^*)$ and 1s-exciton transition energy $\hbar\omega_{ex}(\hbar\omega_{ex}^*)$, and (b) 1s-2s splitting energy $\Delta_{12}(\Delta_{12}^*)$ in a subsurface InGaAs/GaAs quantum well as functions of the thickness L_c of the well-vacuum barrier layer: theory with (solid lines) and without (dashed lines) allowance made for images, and experiment (dots) (after [46]).

ment of the exciton — which is precisely the dependence obtained in experiment (see data points in Fig. 5b).

4. Anisotropy of polariton reflection spectra in layered structures

Properties of layered semiconductor/insulator structures in the vicinity of the polariton resonance are significantly affected by the response nonlocality due to the spatial localization of excitons in thin (compared to the wavelength of light) semiconducting layers. The polarizability of the system can be written in the form [48, 49]

$$\chi_{NL}(\mathbf{q}, \omega; z, z') = \chi^{ex}(\mathbf{q}, \omega) F(z) F(z'), \quad (5)$$

where the exciton form factor $F(z) = \psi^e(z)\psi^h(z)$ is the product of the envelope wave functions of the exciton-forming electron and hole, the coordinate z is directed normal to the layers, and

$$\chi^{ex}(\mathbf{q}, \omega) = \frac{e^2 V_{cv}^2 \Phi(0)^2}{\omega^2} \frac{2\mathcal{E}_{ex}(\mathbf{q})}{\mathcal{E}_{ex}^2(\mathbf{q}) - (\hbar\omega)^2},$$

where ω is the frequency of the electromagnetic wave, and \mathbf{q} is its wave vector in the layer plane, $\mathcal{E}_{ex}(\mathbf{q})$ is the exciton dispersion relation, and V_{cv} is the interband matrix element of velocity. As the polariton resonance is approached, an additional resonant increase in the dielectric susceptibility occurs accordingly the larger field-redistribution effects. For instance, the reflection coefficient becomes strongly dependent on the wave polarization relative to the layers [50]. Such dependences were found experimentally in lead-iodide-based compounds [42] and were adequately described [51] by the Maxwell equations with the susceptibility of the form (5). In the immediate neighbourhood of the exciton resonance, the field distribution depends strongly on the exciton form factor,

which enables the wave function shapes to be examined using then effects like resonance Raman scattering as the base [50].

5. Conclusion

Effects due to the difference in permittivities relating to adjacent regions are considered for nanostructures such as superlattices, semiconductor/insulator quantum wells, sub-surface semiconductor quantum wells, and ‘open’ (free-standing on the semiconductor surface) quantum filaments and dots. In such structures the permittivity difference causes a spatial redistribution of the electric field (for example, in the electromagnetic wave or in the field binding the electron and the hole in an exciton) thus producing dramatic changes in the optical and electronic properties of the nanostructures involved. Examples are the strong linear polarization of emission, absorption and Raman scattering in open quantum filaments, the so-called dielectric enhancement of excitons in semiconductor/insulator or semiconductor/vacuum nanostructures, and the strong anisotropy of polariton reflection spectra.

We have greatly benefited from the collaboration with A B Dzyubenko, L V Keldysh, L V Kulik, G N Mikhaïlova, E A Mulyarov, A M Prokhorov, A L Yablonskiï, J M Calleja, Al L Efros, A Forchel, T Ishihara, F Koch, D Kovalev, and M Rosen. We also thank V S Bagaev, V S Dneprovskii, E A Zhukov, V V Poborchii, A P Silin, R A Suris, and H Mariette for helpful discussions. The present work was supported by an RFBR grant, the RF State Program ‘Solid-State Nanostructure Physics’, and by INTAS grant No 94-2112.

References

- Esaki L, in *Heterojunctions and Semiconductor Superlattices* (Eds G Allan et al.) (Berlin: Springer-Verlag, 1986) p. 12; Bastard G *Wave Mechanics Applied to Semiconductor Heterostructures* (Les Ulis, France: Les Editions de Physique, 1988)
- No consideration is given here to these interesting and important systems; see, for example, in Weisbuch C et al. *Phys. Rev. Lett.* **69** 3314 (1992); Weisbuch C *J. Cryst. Growth* **138** 776 (1994); Ivchenko E I, Nesvizhskii A I, Jorda S *Superlattices and Microstructures* **16** 17 (1994); Koch S W, Jahnke F, Chow W W *Semicond. Sci. Technol.* **10** 739 (1995)
- Nakamura S et al. *Appl. Phys. Lett.* **67** 1868 (1995)
- Kumagai M, Takagahara T *Phys. Rev. B* **40** 12359 (1989); Reichow J et al. *J. Cryst. Growth* **131** 277 (1993); Funato M, Fujita Shizuo, Fujita Shigeo *Jpn. J. Appl. Phys.* **32** 3396 (1993)
- Aktsipetrov O A et al. *Surf. Sci.* **325** 343 (1995)
- Golubkov V V, Ekimov A I, Onushchenko A A *Fiz. Khim. Stekla* **6** 511 (1980); Efros Al L, Efros A L *Fiz. Tekh. Poluprovodn.* **16** 1209 (1982) [*Sov. Phys. Semicond.* **16** 772 (1982)]; Bawendi M G et al. *Phys. Rev. Lett.* **65** 1623 (1990); Ekimov A I, Efros Al L, Onushchenko A A *Solid State Commun.* **88** 947 (1993)
- Poborchii V V, Ivanova M S, Salamatina I A *Superlattices and Microstruct* **16** 133 (1994); Dneprovskii V, Gushina N, Zhukov E *Phys. Lett. A* **204** 59 (1995)
- Canham L T *Appl. Phys. Lett.* **57** 1046 (1990)
- Dreybrodt J et al. *Phys. Rev. B* **48** 14741 (1993); **51** 4657 (1995); Emiliani V *Appl. Phys.* **75** 5114 (1994)
- Gréus C et al. *Appl. Phys. Lett.* **61** 1199 (1992); Ils P et al. *Appl. Phys. Lett.* **64** 496 (1994)
- Gourgon C et al. *J. Cryst. Growth* **138** 590 (1994)
- Gourgon C et al. *Appl. Phys. Lett.* **66** 1635 (1995)
- Kohl M et al. *Phys. Rev. Lett.* **63** 2124 (1989)
- Bockelmann U, Bastard G *Phys. Rev. B* **45** 1688 (1992)
- Gréus C et al. *J. de Phys. IV* **3** 139 (1993)
- Gippius N A et al. *Pis'ma Zh. Eksp. Teor. Fiz.* **59** 527 (1994) [*JETP Lett.* **59** 556 (1994)]; Gippius N A et al. *Superlattices and Microstructures* **16** 165 (1994)
- Lukosz W, Kunz R E *J. Opt. Soc. Am.* **67** 1607 (1977)
- Lavallard P, Rosenbauer M, Gacoin T *Phys. Rev. A* **54** 5450 (1996)
- Ils P et al. *Phys. Rev. B* **51** 4272 (1995)
- Gippius N A et al. *Phys. Status Solidi (b)* **188** 269 (1995); Rubio J et al. *Solid-State Electron.* **40** 707 (1996)
- Bockelmann U *Europhys. Lett.* **16** 601 (1991)
- Andrianov A V et al. *Pis'ma Zh. Eksp. Teor. Fiz.* **58** 427 (1993) [*JETP Lett.* **58** 417 (1993)]
- Lavallard P, Suris R A *Solid State Commun.* **95** 267 (1995)
- Kovalev D et al. *Appl. Phys. Lett.* **67** 1585 (1995)
- Landau L D, Lifshitz E M *Quantum Mechanics — Non-relativistic Theory* (Oxford: Pergamon Press, 1977)
- Rytova N S *Dok. Akad. Nauk SSSR* **631** 118 (1965) [*Sov. Phys. Dokl.* (1965)]
- Chaplik A V, Éntin M V *Zh. Eksp. Teor. Fiz.* **61** 2496 (1971) [*Sov. Phys. JETP* **34** 1335 (1972)]
- Keldysh L V *Pis'ma Zh. Eksp. Teor. Fiz.* **29** 716 (1979) [*JETP Lett.* **29** 658 (1979)]
- Babichenko V S, Keldysh L V, Silin A P *Fiz. Tverd. Tela (Leningrad)* **22** 1238 (1980) [*Sov. Phys. Solid State* **22** 723 (1980)]
- Guseinov R R *Phys. Status Solidi (b)* **125** 237 (1984)
- Fomin V M, Pokatilov E P *Phys. Status Solidi (b)* **136** 187 (1986)
- Andryushin E A, Silin A P *Fiz. Tverd. Tela (Leningrad)* **30** 3253 (1988) [*Sov. Phys. Solid State* **30** 1871 (1988)]
- Hanamura E et al. *Mater. Sci. Eng. B* **1** 255 (1988)
- Tran Thoai D B et al. *Phys. Rev. B* **42** 5906 (1990)
- Wendler L, Hartwig B *J. Phys.: Condens. Matter* **3** 9907 (1991)
- Takagahara T *Phys. Rev. B* **47** 4569 (1993)
- Muljarov E A et al. *Phys. Rev. B* **51** 14370 (1995)
- Silin A P, Andryushin E A *Fiz. Tverd. Tela (Leningrad)* **35** 1947 (1993) [*Sov. Phys. Solid State* **35** 164 (1993)]
- Babaev N A et al. *Pis'ma Zh. Eksp. Teor. Fiz.* **40** 190 (1984) [*JETP Lett.* **40** 952 (1984)]
- Nagapetyan S S et al. *Zh. Neorg. Khim.* **33** 2806 (1988) [*Sov. J. Inorganic Chem.* (1988)]
- Ishihara T, Takahashi J, Goto T *Solid State Commun.* **69** 933 (1989)
- Ishihara T, Takahashi J, Goto T *Phys. Rev. B* **42** 11099 (1990)
- Hong X, Ishihara T, Nurmikko A V *Phys. Rev. B* **45** 6961 (1992)
- Ishihara T *J. Luminescence* **60–61** 269 (1994)
- Mulyarov E A, Tikhodeev S G *Zh. Eksp. Teor. Fiz.* **111** 274 (1997) [*Rus. Phys. JETP* **84** 151 (1997)]
- Kulik L V et al. *Phys. Rev. B* **54** R2335 (1996)
- Yablonskiï A L et al. *Pis'ma Zh. Eksp. Teor. Fiz.* **64** 47 (1996) [*JETP Lett.* **64** 51 (1996)]
- Keldysh L V *Superlattices Microstructures* **4** 637 (1988)
- Ivchenko E L, Kavokin A V *Fiz. Tverd. Tela (Leningrad)* **34** 1815 (1992) [*Sov. Phys. Solid State* **34** 507 (1992)]
- Gippius N A, Tikhodeev S G, Keldysh L V *Superlattices Microstructures* **15** 479 (1994)
- Gippius N A, Muljarov E A, Tikhodeev S G *Phys. Status Solidi (b)* **188** 57 (1995)

PACS number: 73.20.Dx

Momentum dependence of electron state dimensionality in heterostructures

V V Kapaev, Yu V Kopaev, I V Tokatly

1. The electronic properties of quantum wells and wires are usually treated by the method of enveloping wave functions, in which the periodic potential influence in each material is accounted for by an appropriate effective mass in the kinetic energy operator, and interface changes in the dispersion law act as effective potentials.

For quantum wells, the wave vector components (k_z, k_y) are conserved along the layers. Due to the difference in the effective mass components of the adjacent materials the effective potentials depend on k_x, k_y . This may even reverse

the sign of the effective potential, thus converting a potential well to a barrier and vice versa.

2. The wave function in a quantum well may be taken in the form

$$\psi(x, y, z) = Z(z) \exp(ik\rho),$$

where z is the coordinate along the growth axis, ρ lies in the layer plane, and $k = (k_x^2 + k_y^2)^{1/2}$. The Schrödinger equation for $Z(z)$, assuming an isotropic mass for each of the heterostructure-forming layers, is of the form

$$Z''(z) + \frac{2m_n}{\hbar^2} \left(E - \frac{\hbar^2 k^2}{2m_n} - U_n \right) Z(z) = 0, \quad (1)$$

where m_n and U_n are the effective mass and potential in the n th layer. The quantities Z and Z'/m_n are continuous at the layer interfaces. For a single quantum well of thickness d we thus have the following dispersion equation for the bound state energy E :

$$\left(\frac{\alpha_1}{m_1} + \frac{\alpha_2}{m_2} \right) \cos(\alpha d) + \left(\frac{\alpha_1 \alpha_2}{m_1 m_2} \frac{m}{\alpha} - \frac{\alpha}{m} \right) \sin(\alpha d) = 0, \quad (2)$$

where

$$\alpha = \left\{ \frac{2m}{\hbar^2} [E - V_0(k)] \right\}^{1/2}, \quad \alpha_{1,2} = \left\{ \frac{2m_{1,2}}{\hbar^2} [V_{1,2}(k) - E] \right\}^{1/2},$$

here m_1 , m_2 , and m are the effective masses for the left and right barriers and for the well, respectively; in addition

$$V_{1,2}(k) = U_{1,2} + \frac{\hbar^2 k^2}{2m_{1,2}}, \quad V_0(k) = \frac{\hbar^2 k^2}{2m}$$

are the barrier and well potentials for finite k , and U_i are those for $k = 0$.

For $U_1 \neq U_2$, a bound state arises when the well width exceeds the critical value [1]. The asymmetry of a barrier may be characterized by the parameter

$$\beta(k) = \frac{V_2(k) - V_0(k)}{V_1(k) - V_0(k)}.$$

For $m < m_1$, the derivative $\partial\beta(k)/\partial k$ has the same sign as the parameter

$$\alpha = \frac{U_2}{U_1} - \frac{m_2 - m}{m_1 - m} \frac{m_1}{m_2}, \quad (3)$$

i.e. at $\alpha > 0$ ($\alpha < 0$) the system becomes more asymmetric (symmetric) as k increases (we take $U_2 > U_1$ to be specific). If $m > m_1$, the sign of $\partial\beta(k)/\partial k$ is opposite to that of α .

For type I heterostructures typically $m < m_1 < m_2$. In this case at

$$k_i = \left[\frac{2U_i m m_i}{\hbar^2 (m_i - m)} \right]^{1/2}$$

either the left ($i = 1$) or the right ($i = 2$) barrier disappears, whereas for

$$k_s = \left[\frac{2(U_2 - U_1) m_1 m_2}{\hbar^2 (m_2 - m_1)} \right]^{1/2}$$

the barrier heights become equal. The mutual positions of k_1 , k_2 , and k_s are determined by the sign of α . For $\alpha > 0$ we have $k_1 < k_s < k_2$, whereas for $\alpha < 0 - k_s$, the inequality $k_2 < k_1$ holds.

The asymmetry of the barriers results in the disappearance of the bound state at k_c values substantially less than k_1 and for k_2 . To determine k_c , one has to solve (2) for k under the additional condition $E = V_i(k_{ci})$. For $\alpha > 0$ there exists one critical value k_{c1} , which obeys the equation

$$\frac{d}{\lambda} = \frac{1}{2\pi\tilde{\alpha}} \arctan \left\{ \frac{m}{m_2} [\beta(k_{c1}) - 1] \right\}^{1/2} + \frac{n}{2\tilde{\alpha}}, \quad (4)$$

where

$$\tilde{\alpha} = \left[1 - \left(\frac{k_{c1}}{k_0} \right)^2 \left(1 - \frac{m}{m_1} \right) \right]^{1/2},$$

$$k_0 = \frac{2\pi}{\lambda}, \quad \lambda = \left(\frac{2\pi^2 \hbar^2}{2mU_1} \right)^{1/2},$$

$n = 0, 1, \dots$ specifies the subband. For $\alpha < 0$ there exists a second value of k_{c2} , which is obtained from (4) by setting

$$\tilde{\alpha} = \left[\frac{U_2}{U_1} - \left(\frac{k_{c2}}{k_0} \right)^2 \left(1 - \frac{m}{m_2} \right) \right]^{1/2},$$

then interchanging $m_1 \leftrightarrow m_2$, and replacing β by $1/\beta$.

Figure 1 illustrates the $d(k)$ state diagram describing the boundary between the bound (2D) and unbound (3D) states. The lines 1, 2, and 3 correspond to the condition $E = V_1$, and the lines 2' and 3' to $E = V_2$. The line 1 suits to the case $\alpha > 0$. The bound state exists both above and below this line. For $d < d_{c1}$, it is absent for any k . For $d > d_{c1}$, it occurs in the interval $0 < k < k_{c1}$, the value of k_{c1} increasing from zero to k_1 with a rise in d . For symmetrical barriers, the bound state disappears at $k_c = k_1$ independent of d . The dependence $E(k)$ for $d > d_1$ is shown in insert (a) to Fig. 1, the solid and dashed lines illustrating the 2D- and 3D-states, respectively.

The lines 2 and 2' correspond to $E = V_1$ and $E = V_2$ for $\alpha < 0$; the insert (b), to the case $d < d_{c2}$; and (c), to $d > d_{c2}$. For $\alpha < 0$ the dependence $d(k_c)$ may have a maximum (line 3 in Fig. 1). In this case, in the narrow layer-thickness range

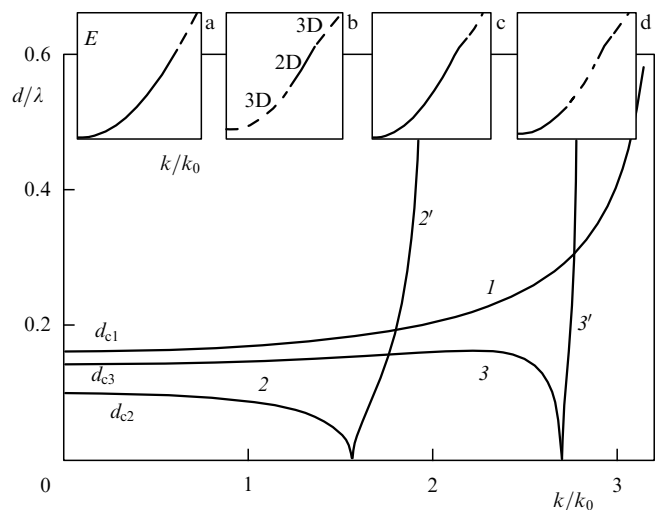


Figure 1. Quantum well phase diagram. Lines 1, 2, and 3 correspond to the condition $E = V_1$, 2' and 3', to $E = V_2$; $m_1 = 1.1m$, $m_2 = 2.0m$ for $U_2/U_1 = 6$ (line 1), 4 (2, 2'), and 2 (3, 3'). Inserts display dispersion lines $E(k)$: (a) for line 1; (b, c) for 2 and 2'; (d) for 3 and 3'.

$d_{c2} < d < d_{\max}$ there exist three critical values of k_c (see insert (d)). The disappearance of the state as $k \rightarrow k_{c1}$ is due to the fact that, in spite of system symmetrization, the well depth decreases faster than the barrier heights become equal.

If the mass in the well exceeds the barrier masses, the reverse situation is possible in which a bound state arises as an asymmetry increases due to the fact that the well depth increases faster than the barrier heights difference.

The application of an electric field F_z modifies the relation between the barrier potentials while leaving unchanged the effective masses in the layers. The masses and potentials thus ‘decouple,’ making α a controllable parameter. If at the higher barrier the voltage ΔU is positive we may have a transition from $\alpha > 0$ to $\alpha < 0$, whereas for $\Delta U < 0$ a reverse transition is possible. We thus see that in structures of the same composition all the situations discussed above may be realized.

In single-well structures the probability of finding an electron in a well w vanishes rather rapidly as one approaches the turning point. Far away from k_c , w depends weakly on k . In multiwell structures a situation may occur in which changing k redistributes the probabilities w_i between the wells quite significantly for k values much less than k_c . This takes place in systems near the dimensional quantization level resonance. In this case a change in the barrier heights with k significantly modifies the well-to-well electron tunnelling conditions. With increasing k , a transition from one 2D-state to another, with a different electron localization, takes place. Thus, the electron density can be redispersed by increasing k .

The fact that the effective mass in the well differs from those in the barriers has the consequence that the law of dispersion $E(k)$ deviates from being parabolic even if the initial dispersion’s not being parabolic in the heterostructure components is neglected. The effective mass $\mu = \hbar^2(\partial^2 E/\partial k^2)^{-1}$ for the motion along the layers at $k = 0$ becomes different for various subbands, varying from the effective well mass m in deep subbands to the mass of one of the barriers in shallow subbands. In multiwell structures an anomalous behaviour is observed, when μ for a low lying subband may exceed that for a higher energy one. Most interestingly, the function $E(k)$ changes its curvature near the turning points thus making the effective mass negative over a certain k region.

The following are some of the possibilities for detecting the termination (emergence) lines in the bound state momentum space (k_x, k_y) :

(1) The nature of electron motion in a magnetic field will change (see below), according to whether the field is oriented along the layers or z -axis. Depending on the position of the termination line and the Fermi line relative to each other, oscillations in the kinetic and thermodynamic quantities with magnetic field will correspond to either the two-dimensional or three-dimensional case. The quantum Hall effect must disappear upon the 2D–3D transformation, and the transformation itself can be observed on one and the same sample by using electric field to control the carrier density and termination line positions.

(2) Upon the electric-field-induced 2D–3D transformation a change in the nature of phase transformations may occur. For example, ferromagnetism may disappear if the ferromagnetic ordering in the material is determined by the carrier-assisted indirect exchange interaction between magnetic ions located in the quantum wells.

(3) Because the coupling energy for the 2D case is 4 times that for the 3D case, a sharp change in the exciton or impurity-state coupling energies may be observed as the sharp position of the termination (emergence) line is altered. This sharp change will occur when the termination (emergence) line momentum and the corresponding inverse Bohr radius become equal.

(4) For superlattices of asymmetric quantum wells, the inverse Franz–Keldysh effect may be observed, in which the forbidden miniband widens under the action of the field F_z as a result of the 3D–2D transformation. Due to the formation of bound 2D states, the overlap integral of wave functions from neighbouring quantum wells decreases and the allowed minibands therefore become narrower.

(5) A direct observation of the 2D–3D transformation under a lateral electric field is yet another possibility. The 2D–3D defocusing (or 3D–2D focusing) of electronic states which takes place in this case may be seen in transient phenomena. In time-resolution experiments, the shift in the exciton line position will be determined by the change in the coupling energy.

(6) A system of two quantum wells, one of them with asymmetric barriers, may prove useful for reducing the threshold current in the quantum cascade laser, whose lasing frequency depends on the energy separation between the subband minima of neighbouring wells. If the lower subband corresponds to the asymmetric well, its termination line may be well below the minimum of the upper subband, with the result that the one-phonon intersubband relaxation will be suppressed and the threshold current reduced.

3. Let us consider the behaviour of electrons in a quantum well with asymmetric barriers subjected to a quantizing magnetic field \mathbf{B} parallel to the growth axis z of the structure. We take the zero of energy to coincide with the lower (right) barrier U_1 and place the left boundary of the well at $z = 0$. Letting now $-U_1 \equiv -V$ for the well depth and $U_2 - U_1 \equiv U$ for the left barrier height, the Schrödinger equation takes the form

$$\left\{ \frac{\hat{k}_z^2 + [\hat{k} - (e/c)\mathbf{A}(\rho)]^2}{2m(z)} + u(z) \right\} \psi(\rho, z) = \varepsilon \psi(\rho, z), \quad (5)$$

where

$$\frac{1}{m(z)} = \frac{1}{m_2} \theta(-z) + \frac{1}{m} [\theta(z) - \theta(z-d)] + \frac{1}{m_1} \theta(z-d),$$

$$u(z) = U\theta(-z) - V[\theta(z) - \theta(z-d)]. \quad (6)$$

In (5), \hat{k} denotes the momentum operator component in the xy -plane, and the vector-potential $\mathbf{A}(\rho)$ is related to magnetic field in the standard way, so that $\mathbf{B} = \partial_x A_y - \partial_y A_x$. For a uniform magnetic field the variables z and ρ in (5) separate to give

$$\psi_v(\rho, z) = \chi_v(z) \phi_v(\rho), \quad (7)$$

with $\phi_v(\rho)$ obeying

$$\frac{1}{2} \left[\hat{k} - \frac{e}{c} \mathbf{A}(\rho) \right]^2 \phi_v(\rho) = \xi_v \phi_v(\rho). \quad (8)$$

The eigenvalues ξ_v in (8) are

$$\xi_v = \frac{1}{l_B^2} \left(v + \frac{1}{2} \right), \quad v = 0, 1, 2, \dots,$$

$$\frac{1}{l_B^2} = \frac{eB}{\hbar c}. \quad (9)$$

and the equation for the function $\chi_v(z)$ is

$$\left[\frac{\hbar^2 k_z^2 + 2\xi_v}{2m(z)} + u(z) \right] \chi_v(z) = \varepsilon_v \chi_v(z). \quad (10)$$

The dependence $m(z)$ in (10) yields the magnetic-field dependence of the effective potential. In particular, the effective well depth V_v for the v th Landau subband is found to be

$$V_v = V - \left(\frac{1}{m} - \frac{1}{m_1} \right) \xi_v \equiv V - (\omega_W - \omega_R) \left(v + \frac{1}{2} \right), \quad (11)$$

and the effective height of the left barrier is

$$U_v = U - \left(\frac{1}{m_1} - \frac{1}{m_2} \right) \xi_v \equiv U - (\omega_R - \omega_L) \left(v + \frac{1}{2} \right), \quad (12)$$

where ω_W and ω_R, ω_L are the cyclotron frequencies in the well and in the barriers, respectively.

Thus we find, for the eigenvalues of (10), the expression

$$\varepsilon_v^{2D} = \hbar\omega_R \left(v + \frac{1}{2} \right) - \frac{\kappa_{Rv}^2}{2m_1}, \quad (13)$$

$$\kappa_{Rv} = \frac{2m_1 V_v d}{1 - m_1/m_2} \left\{ 1 - \sqrt{\frac{m_1}{m_2} \left[1 + \left(1 - \frac{m_1}{m_2} \right) \frac{U_v}{2m_1 (V_v d)^2} \right]} \right\}. \quad (14)$$

For symmetrical barriers ($U = 0, m_1 = m_2 \equiv m_B, \omega_R = \omega_L \equiv \omega_B$) from (13) and (14) we obtain

$$\varepsilon_v^{2D} = \hbar\omega_B \left(v + \frac{1}{2} \right) - \frac{1}{2} m_B (Vd)^2 \left[1 - \frac{\omega_B}{\Omega_e} \left(v + \frac{1}{2} \right) \right]^2, \quad (15)$$

where

$$\Omega_e = \frac{V_m}{\hbar(m_B - m)}.$$

Equation (15) implies that two-dimensional energy levels exist until the transverse motion energy $\hbar\omega_B(v + 1/2)$ becomes equal to $\hbar\Omega_e$, when the effective well potential V_v , Eq. (11), comes to nought. Thus, for every level v there exists a critical magnetic field B_c^v above which the v th 2D Landau level moves to a 3D Landau subband:

$$B_c^v = \frac{m m_B}{m_B - m} \frac{cV}{e\hbar(v + 1/2)}. \quad (16)$$

Notice that in the magnetic field B_c^0 the last level (i.e. the ground level with $v = 0$) disappears.

An important point to note about the energy spectrum (15) is that the Landau levels are not equidistant. This can be seen either directly in optical experiments or from the violation of the inverse-magnetic-field periodicity of Shubnikov-de Haas magnetoresistance oscillations.

In the case of asymmetric barriers, a more complex and diverse behaviour is displayed by the system. Depending on the relation between the parameters

$$\alpha = \frac{m_1}{8m_2} \frac{1 - (m_1/m_2)V}{m_1/m - 1} \frac{V}{\varepsilon_0}, \quad \beta = \frac{1}{4} \frac{m_1 U}{m_2 \varepsilon_0} \quad (17)$$

($\varepsilon_0 = 0.5m_1(Vd)^2$ being a level in a shallow symmetric well), five different types of behaviour are possible for the 2D spectrum of electrons in a magnetic field.

The (α, β) phase diagram for these five regions is shown in Fig. 2. The system behaviour in region 1 is qualitatively the same as that in the symmetric case: 2D states exist at $B = 0$ and disappear when $\omega_R(v + 1/2) > \Omega_e$, which implies the vanishing of the effective potential (11).

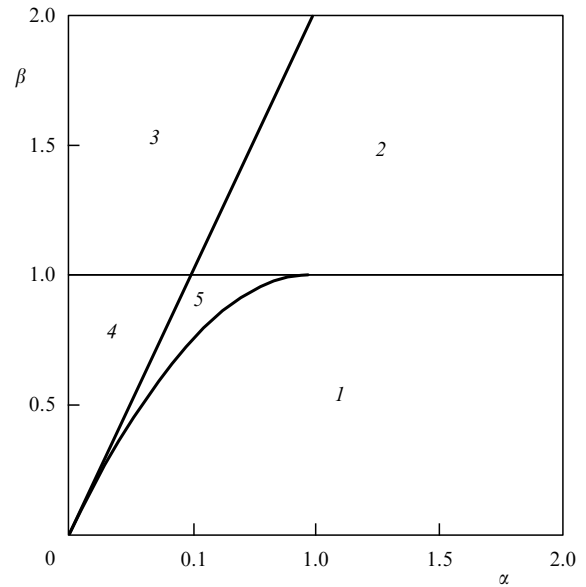


Figure 2. Phase diagram in variables (α, β) for a quantum well with asymmetric barriers in a magnetic field.

In region 2, 2D states are absent in zero field but do exist in the interval

$$0 < y_+ \Omega_e < \omega_R \left(v + \frac{1}{2} \right) < \Omega_e,$$

$$y_{\pm} = 1 - \alpha \pm \sqrt{(1 - \alpha)^2 - 1 + \beta}.$$

There is an analogy here to case ‘b’ of Fig. 1.

In region 3, 2D Landau states are absent for any magnetic fields, analogous to case $d < d_{c1}$ for line 1 in Fig. 1. In region 4 of Fig. 2, 2D states exist in the interval

$$0 < \omega_R \left(v + \frac{1}{2} \right) < y_- \Omega_e < \Omega_e.$$

Here 2D Landau levels may have a much narrower existence domain compared to a symmetric structure. In Fig. 1, line 2 for $d > d_{c2}$ corresponds to this case.

A very nontrivial behaviour is seen in region 5. Here 2D levels exist in the zero field but as the field is increased, they disappear at $\omega_R(v + 1/2) \geq \Omega_e y_-$ and then reappear in the interval $\Omega_e y_+ < \omega_R(v + 1/2) < \Omega_e$. This situation is analogous to case ‘d’ in Fig. 1.

There is a significant difference here, compared with the case of identical well and barrier masses, in the way the occupation of 2D Landau levels varies with the magnetic field. In the identical case, at $B = 0$ the number n_0 of 2D states lying below 3D states is

$$n_0 = \frac{m}{\hbar^2 \pi} \varepsilon_0.$$

An applied magnetic field produces Landau levels, each of which has a degeneracy (including spin)

$$n_L = \frac{m}{\pi \hbar} \omega_c.$$

The number of levels below the zeroth 3D Landau subband ($E_0 = \hbar \omega_c / 2$) is $\nu = [\varepsilon_0 / \hbar \omega_c]$ and hence the total number of states in these levels is

$$\frac{m}{\hbar \pi} \omega_c \left[\frac{\varepsilon_0}{\hbar \omega_c} \right] \leq n_0.$$

Thus, if the total number of particles $n < n_0$ (for $B = 0$ all of them were in the 2D region) then the applied magnetic field does not alter this condition and all the particles are two-dimensional. In other words, as the field increases, the ν th 2D Landau levels one by one cross the bottom of the zeroth 3D Landau subband, but given $n < n_0$ they always prove to be empty when crossing the bottom. Thus the 3D subband is always empty.

Including the mass difference alters the situation dramatically. For zero field, the number n_0 of 2D states lying below the minimum of 3D states equals $n_0 = (m/\pi \hbar) \Omega(0)$, where $\Omega(0)$ is the solution to the equation

$$\Omega(0) - \varepsilon_0 \left(\frac{\Omega(0)}{\Omega_0} \right) = 0.$$

In region 1, $\Omega_0 = \Omega_c$ and in regions 4 and 5, $\Omega_0 = \Omega_{c\nu}$. Let n_b^v (n_a^v) be the number of 2D states immediately before (after) the ν th 2D level crosses the zeroth 3D subband, so that

$$n_b^v = \frac{m}{\hbar \pi} \omega_{\nu} (\nu + 1), \quad n_a^v = \frac{m}{\hbar \pi} \omega_{\nu} \nu$$

(ω_{ν} corresponds to the crossing field). Then from Eqs. (13) and (14), it can be shown that the sequences of n_b^v and n_a^v numbers are arranged as follows:

$$\begin{aligned} \dots > n_b^{v-1} > n_b^v > n_b^{v+1} > \dots > n_0, \quad \lim_{v \rightarrow \infty} n_b^v = n_0, \\ n_0 > \dots > n_a^{v+1} > n_a^v > n_a^{v-1} > \dots, \quad \lim_{v \rightarrow \infty} n_a^v = n_0. \end{aligned} \quad (18)$$

Thus the sequences n_b^v and n_a^v converge to n_0 from above and below, respectively, and for any number of particles $n < n_0$ one can always indicate ν such that $n_a^{v+1} > n > n_a^v$. Notice that, starting from ν , the 2D levels are partially filled when crossing the bottom of the lowest 3D subband and that they become progressively unfilled so as the 3D pool of carriers continues to form. Owing to this pool, and up to the point it becomes fully depleted with the increasing field, the next level will remain completely filled. Because the pool is depleted before the $(\nu - 1)$ th level approaches the 3D states, a step-by-step change in the 2D Landau level filling will take place even when the number of particles in, rather than the chemical potential of, the system is fixed. Experimentally, this will show up in that the integral quantum Hall steps will broaden starting from a certain field dependent on the number of

particles in the system. Clearly, as the field increases above $B_c^{(0)}$, the last 2D level will disappear thus making the quantum Hall effect impossible.

In more complex heterostructures, a change in topology due to a change in the longitudinal momentum is possible, for example, when two wells transform into two barriers or a transition from a ‘well-in-a-well’ structure to two wells separated by a barrier takes place. Similar topology changes will also result from magnetic field variation. Thus, one might expect new phenomena of the quantum Hall effect to be detected in such structures.

The possibility of a 2D–3D transformation at relatively small longitudinal momenta in a magnetic field is not limited to the quantum wells with strongly asymmetric barriers as discussed above. Other candidates are symmetric heterostructures which, together with a small position difference between the conduction band edge (for electrons) and the valence band edge (for holes), also have very different gap widths and hence very different effective masses. The former situation applies, for example, in the GaAs/GaN heterostructure [2], the latter, in InGaAs/AlGaAs [3].

This work was supported by the Russian Foundation for Basic Research, by INTAS, and by the ‘Solid State Nanoscale Physics’ Program.

References

1. Landau L D, Lifshitz E M *Quantum Mechanics — Non-relativistic Theory* (Oxford: Pergamon Press, 1977)
2. As D J et al. *Phys. Rev. B* **54** R11118 (1996)
3. Kavokin A V et al. *Phys. Rev. B* **54** R11076 (1996)

PACS numbers: 73.40.Gk, 73.40.Rw

An experimental study of charge effects in ultrasmall tunnel junctions

V A Krupenin, S V Lotkhov,
Yu A Pashkin, D E Presnov

1. Introduction

One major technological achievement in today’s progress toward miniaturization is that device elements less than one tenth of a micron in size can now be fabricated in a controllable way. The novel and spectacular effects exhibited by such devices have given rise to the so-called ‘nanophysics,’ an entirely new direction in modern science. Part of it, single-electronics, is concerned with effects involving the discrete transport of charge through low-self-capacity structures. The orthodox theory of single-electron tunnelling, originally intended for tunnel junctions [1], was later extended to other structures as well and has been confirmed in many experiments [2]. Interest in the charge effects stems from their high promise for fundamentally novel recording-property devices.

2. Technology

Metal-insulator-metal tunnel junctions were fabricated using the well-known oblique angle deposition technique [3]. This technique has a soft-mask [4] and a rigid-mask variety [5]. In the former, a two-layer resist deposited on the substrate is first irradiated by an electron beam and then selectively developed to form the desired pattern. The mask proper is the upper

resist, through which both the lower and upper tunnel junction electrodes are evaporated at different angles. Evaporating the upper electrode is preceded by the oxidation of the lower one in an oxygen atmosphere, thus making the technique self-compatible. As an electrode material, any metal with a low evaporation temperature, good oxidizability, and low graininess — for example, aluminium — may be used. The resulting lines are typically about 0.1 μm in width, and the tunnel junction that forms at the intersection of the upper and lower electrodes is about 0.01 μm^2 in area.

In the rigid-mask variety, a three-layer (electron resist – a germanium – electron resist) structure is deposited on the substrate. Following electron beam irradiation and the development process, the desired pattern develops in the upper layer of the resist. The pattern is then transferred to the germanium layer using a plasmochemical etching technique, and part of the resist is removed from the lower layer during the process of anisotropic and isotropic etching in oxygen. This is a more effective technique as far as complex structures are concerned.

To ensure high external impedance, an additional deposition procedure was carried out in which, following chromium deposition perpendicular to the substrate, properly oxidized aluminium was deposited at two different angles. Chromium is also compatible with our resists whose film shows good reproducibility properties. With a 60 Å-thick chromium film having a resistivity of 2 $\text{k}\Omega \square^{-1}$, an external circuit resistance conservatively in excess of the quantized resistance $R_Q \equiv h/4e^2 \simeq 6.5 \text{ k}\Omega$ was achieved.

3. Single tunnel junctions

The theory of correlated tunnelling predicts single-electron and Bloch oscillations to occur in single-tunnel junctions connected to a current source [1]. Experimentally this requires that the external electrical circuit has a high impedance, which is achieved by introducing high-resistance thin-film resistors into the measuring electrodes in the immediate vicinity of the junction. Both types of coherent oscillations were found in Ref. [6] using high-frequency irradiation of the single-tunnel junctions to detect oscillations. When the natural vibration frequency equalled that of the irradiating signal, voltage steps arose on the current-voltage characteristic of the transition. For the same irradiation frequency, the step separation in the Bloch oscillations is twice that in the single-electron oscillations. Using this technique, Bloch oscillations in a chain of two Josephson junctions have been detected [7].

The temperature dependence of the linewidth of the Bloch oscillations in Josephson tunnel junctions has been measured in [8]. It is found that at low temperatures the linewidth, instead of following a linear temperature dependence as predicted by theory, tends to saturate, the level of saturation being dependent on the junction current. This behaviour is nicely explained in qualitative way by a simple model involving the electron superheating in thin-film chromium resistors.

Kuzmin et al. [9] investigated experimentally the effect of the critical current passing through a small high-external-impedance Josephson junction on the ratio of the charge to the Josephson transition energy. In the weak coupling region, it is shown that the critical current is determined by Zener tunnelling and that the experimental data are in good quantitative agreement with the theory of Zener tunnelling if Ohmic dissipation is taken into account.

4. Single-electron transistors

The single-electron transistor consists of two in-series tunnel junctions and its central island potential can be controlled by the gate voltage. If thermal and quantum fluctuations are small, then owing to the spatial correlations between tunnelling events in both the junctions, the current-voltage characteristic of the device can be periodically modulated using the gate voltage, with the period corresponding to a single electron charge [1] and the charge sensitivity of the system being a fraction of this charge [10]. For the transistor with a nonzero Josephson coupling, a $2e$ -periodic current-voltage characteristic modulation is predicted by the theory [1], which has also been examined experimentally [11, 12].

There is a good deal of experimental evidence [13–20] to show that the limiting values of the basic characteristics of single-electron devices (the charge sensitivity of the electrometer, the time of electron storage in the charge trap, the turnstile and pump accuracy) depend significantly on the fluctuation level of the electric field generated by the immediate electrodynamic surrounding of the junction. Isolated from the electrode by high-resistance tunnel junctions, the conducting islands in the surrounding field acquire a random background potential, or induced charge, usually referred to as the background effective charge of the island. Fluctuations of this charge play a dominant role in the low-frequency ($< 10\text{--}100 \text{ Hz}$) portion of the noise spectrum of single-electron structures. Therefore, an understanding of noise production and localization mechanisms and the search for noise reduction approaches are of extreme importance for the design and practical application of specific single-electron devices.

From experiments on single-electron transistor noise it is known that:

(1) the fluctuation spectrum of the background charge usually has a shape similar to $1/f$ and its cutoff frequency is of the order of 1 kHz [13–21];

(2) the charge noise level at 10 kHz is $10^{-3}\text{--}10^{-4} e \text{ Hz}^{-1/2}$ [13–17, 20, 21] and is virtually temperature independent for $T < 300 \text{ mK}$ [17, 19];

(3) telegraph noise fluctuations of up to 0.1–0.2 e involving random switching between 2, 3 and more levels have been observed [13, 14, 16, 19];

(4) the noise properties of chromium-based transistors with a thermally oxidized tunnel barrier are identical to those of their aluminium-based counterparts [20].

Based on the available experimental data we believe that background charge fluctuations are to a large extent caused by individual electrons randomly walking between charge traps formed due to structural defects present in the dielectric sublayer and to the natural oxide of the metallic islands of the tunnel structure. Also, the partial localization of fluctuation sources in the tunnel junction barrier cannot be ruled out.

The transistors studied varied in the size of their central islands. The structures were fabricated on a Si substrate with a 200-nm AlO_x layer using a magnetron evaporation technique. The measured noise level at 10 Hz is $(2\text{--}3) \times 10^{-4} e \text{ Hz}^{-1/2}$ and $(5\text{--}6) \times 10^{-4} e \text{ Hz}^{-1/2}$ for islands about 200 nm and 500–600 nm in size, respectively. The observed increase in the noise level with island size (see also [15]) may be attributed to the increase in the effective capacitive coupling between the island and the noise sources (presumably local charge traps) in the electrodynamic surrounding.

In transistors fabricated on a dielectric AlO_x 100-nm sublayer separated by a metal screen from the Si substrate,

both the noise level and the shape of the charge fluctuation spectrum are virtually the same as those measured for the no-screen case, which reduces the distance at which fluctuation sources are felt to less than 100 nm.

Direct evidence for the existence of noise sources outside the tunnel barrier in single-electron structures comes from an experimental study [18] of fluctuation mutual correlations in a system of two transistors a short distance apart. For transistors fabricated on various dielectric sublayers (200-nm AlO_x, thermally grown 500-nm SiO₂), the pair correlation coefficient was 20–40% for capacitive coupling coefficients as low as 5–15%. The results of this experiment suggest that the noise sources which possibly exist in the tunnel barrier and which only affect the background charge of the adjacent island, do not dominate the situation and contribute about as much as or even less than the sources located in the dielectric sublayer.

5. Single-electron trap

Recently, the confinement of single electrons in a single-electron trap was demonstrated [22–25]. The trap used was a chain of small-area ($0.1 \times 0.1 \mu\text{m}^2$) tunnel junctions connected to a conducting (or ‘memory’) island located in the electrostatic field of the control electrode. Because the electron energy at an intermediate island greatly exceeds its energy when at the memory island or the external electrode, an electrostatic barrier arises, capable of holding a small integer (positive or negative) number of extra electrons on this particular island. Owing to the barrier, the amount of charge isolated on the memory island depends hysteretically on the gate voltage. Thus, for the same gate voltage within the hysteresis loop, this charge may assume various values depending on its previous history which differ by multiples of the electron charge. A potential application for such charge states is as a logical level, and for the system itself, as a single-electron memory cell.

The width of the hysteresis loop is inherently related to the length of time the charge state withstands destructive factors such as thermal tunnelling activation [24], the co-tunnelling mechanism [26], etc. Although the experimentally examined times of electron storage are of the order of 8 to 12 hours [24, 25], still this is well below the theoretical predictions. In Ref. [25], such factors were investigated as the drift of the background effective charge and the backaction of the current through the electrometer indicating the state of the memory island charge. It is found that under static observation conditions one and the same hysteresis loop may narrow by almost a half with the passage of time, and an increase in the electrometer current from 5 to 300 pA is equivalent to increasing the sample temperature from 35 to 250 mK. The backaction of the electrometer is possibly due to the exciting effect caused by the wideband telegraph-type voltage noise at the electrometer’s central island.

6. Conclusion

The experimental results on single-electron effects in the metal thin-film tunnel junctions are briefly reviewed.

Experimental research on charge effects in ultrasmall tunnel junctions is currently receiving support from RFBR and the ‘Solid-State Nanostructure Physics’ Program.

References

1. Averin D V, Likharev K K, in *Mesoscopic Phenomena in Solids* (Eds B L Altshuler, P A Lee, R A Webb) (Amsterdam: Elsevier, 1991) p. 173
2. Grabert H, Devoret M H (Eds) *Single Charge Tunnelling* (New York: Plenum Press, 1992)
3. Dolan G J *Appl. Phys. Lett.* **31** 337 (1997)
4. Delsing P, PhD Thesis (Göteborg, Sweden: Chalmers Univ. Techn., 1990)
5. Geerlings L J PhD Thesis (Delft, Netherlands: Delft Univ. Techn., 1989)
6. Kuzmin L S, Pashkin Yu A *Physica B* **194–196** 1713 (1994)
7. Kuzmin L S, Pashkin Yu A, Claesson T *Supercond. Sci. Technol.* **7** 324 (1994)
8. Kuzmin L S et al. *Physica B* **203** 376 (1994)
9. Kuzmin L S et al. *Phys. Rev. B* **54** 10074 (1996)
10. Korotkov A N et al., in *Single Electron Tunnelling and Mesoscopic Devices* (Eds H Koch, H Lubbig) (Berlin: Springer-Verlag, 1992) p. 45
11. Pashkin Yu A et al. *Physica B* **194–196** 1049 (1994)
12. Haviland D B, Pashkin Yu A, Kuzmin L S *Physica B* **203** 347 (1994)
13. Zimmerli G et al. *Appl. Phys. Lett.* **61** 237 (1992)
14. Zimmerli G, Kautz R L, Martinis J M *Appl. Phys. Lett.* **61** 2616 (1992)
15. Visscher E H et al. *Appl. Phys. Lett.* **66** 305 (1995)
16. Verbrugh S M et al. *J. Appl. Phys.* **78** 2830 (1995)
17. Martinis J M, Nahum M, Jensen H D *Phys. Rev. Lett.* **72** 904 (1994)
18. Ahlers F-J et al. *Phys. Rev. B* **53** 13682 (1996)
19. Ahlers F-J et al., in *Digest of the Conf. on Precision Electromagnetic Measur.* (CPEM '96) (Braunschweig, Germany, 1996) p. 507
20. Kuzmin L S et al. *Appl. Phys. Lett.* **68** 2902 (1996)
21. Song D et al. *IEEE Trans. Appl. Supercond.* **5** 3085 (1995)
22. Lafarge P et al. *C. R. Acad. Sci. Paris* **314** 883 (1992)
23. Nakazato K, Blaikie R J, Ahmed H J. *Appl. Phys.* **75** 5123 (1994)
24. Lukens J E et al. *Physica B* **203** 354 (1994)
25. Krupenin V A, Lotkhov S V, Presnov D E *Zh. Eksp. Teor. Fiz.* **111** 344 (1997) [*Rus. Phys. JETP* **84** 190 (1997)]
26. Averin D V, Odintsov A A *Phys. Lett. A* **140** 251 (1989)